

Using reservoir computing to construct scarred wavefunctions

L. Domingo,^{1,2,3,*} J. Borondo,^{4,5,†} and F. Borondo^{1,‡}

¹*Departamento de Química; Universidad Autónoma de Madrid; Cantoblanco - 28049 Madrid, Spain*

²*Grupo de Sistemas Complejos; Universidad Politécnica de Madrid; 28035 Madrid, Spain*

³*Instituto de Ciencias Matemáticas (ICMAT); Campus de Cantoblanco; Nicolás Cabrera, 13-15; 28049 Madrid, Spain*

⁴*Departamento de Gestión Empresarial; Universidad Pontificia de Comillas; Madrid, Spain*

⁵*AgrowingData, Almería, Spain*

(Dated: January 22, 2024)

Scar theory is one of the fundamental pillars in the field of quantum chaos, and scarred functions a superb tool to carry out studies in it. Several methods, usually semiclassical, have been described to cope with these two phenomena. In this paper, we present an alternative method, based on the novel machine learning algorithm known as Reservoir Computing, to calculate such scarred wavefunctions together with the associated eigenstates of the system. The resulting methodology achieves outstanding accuracy while reducing execution times by a factor of ten. As an illustration of the effectiveness of this method, we apply it to the widespread chaotic two-dimensional coupled quartic oscillator.

I. INTRODUCTION

At the end of the last century, significant attention was paid to the correspondence between classical and quantum dynamics, particularly in scenarios in which classical chaos dominates [1]. Over time, this evolution gave rise to the field of quantum chaos, which explores how the principles of quantum mechanics apply to classically chaotic systems, or how classical chaos manifests in the quantum world [2]. Two main pillars in the field emerged. First, Bohigas, Giannoni and Schmit [3] found that the level fluctuations of the quantum Sinai's billiard is consistent with the predictions of the Gaussian orthogonal ensemble of random matrices, thus reinforcing the belief that level fluctuation laws are universal. Second, Heller [4] coined the term scar to describe the increase of the probability density that some eigenfunctions exhibit along unstable periodic orbits (POs) of a classically chaotic system. This property came as a surprise since, even though the chaotic classical dynamics cause the classical trajectories to deviate from the POs, many eigenfunctions tend to concentrate near those POs. Later, this definition [5] was generalized resulting in the so-called scarred functions [6, 7], which are not only localized along the PO in configuration space, but also along its invariant manifolds in the phase space [8]. More recently, other interesting perspectives were brought up on the issue. Among them, the use of Loschmidt echoes or fidelity functions [9], out-of-time-order correlators [10], or Krylov operators [11] deserve special consideration.

The scarring phenomenon plays a central role in the study of the correspondence between classical and quantum mechanics in the presence of chaos. For example, scar functions have been used to understand the properties of eigenstates in quantum chaotic systems, since they

form an efficient basis set for calculation of the eigenstates of such systems [5, 8, 12–14].

In the field of machine learning, many algorithms have been designed to predict the time evolution of dynamical systems [15, 16]. A particularly relevant algorithm for this task is called Reservoir Computing (RC), which has proven very useful in chaotic time series prediction [17–19]. The underlying idea is that a well-trained reservoir can reproduce the attractor of the originating chaotic dynamics. Apart from its excellent performance in predicting the input-output dynamics, because of its simple training strategy, it is usually computationally more efficient than other popular machine learning algorithms. In a previous work [20], we provided a method to adapt the classical RC algorithm to perform the time evolution of a quantum wavefunction in time, under the effect of a certain Hamiltonian. The performance of this method was illustrated by integrating the time-dependent Schrödinger equation for some simple 1D and 2D quantum systems, such as the harmonic oscillator and the Morse Hamiltonian.

In this work, we apply this method to a more complex and realistic quantum system, the coupled quartic oscillator, which has been of great interest in the field of quantum chaos [8, 21, 22]. The key idea is to start from a suitable initial wavepacket at a certain energy, and the use of RC to propagate this state in time. From the time evolution of the wavefunction, we can obtain the energy spectrum and the eigenstates of the system around the same energy as the initial state. This method also allows us to obtain the scarred functions of the quantum chaotic system. Similar studies have been recently reported [23] using the Hénon-Heiles 2D potential as a model for molecular vibrations.

The organization of this paper is as follows. Section II describes the coupled quartic oscillator, the quantum system studied in this work, and the methods used in our study. In particular, Sect. IIF presents the original formalism of RC, and in Sect. IIG we describe the adaptations that have to be made to integrate the Schrödinger

* E-mail address: laia.domingo@icmat.es

† E-mail address: jborondo@gmail.com

‡ E-mail address: f.borondo@uam.es

equation. The corresponding results are presented in Sect. III. Finally, Sect. IV ends the paper by summarizing the main conclusions of the present work.

II. SYSTEM AND METHODS

A. System: the two-dimensional coupled quartic oscillator

The system that we have chosen to study is the dynamics of a unit mass particle moving in a two-dimensional coupled quartic potential described with the following Hamiltonian

$$H(x, y, p_x, p_y) = \frac{1}{2} (p_x^2 + p_y^2) + \frac{1}{2} x^2 y^2 + \frac{\epsilon}{4} (x^4 + y^4), \quad (1)$$

with $\epsilon = 0.01$. The potential of this system is analytic and induces very chaotic dynamics [22, 24], reasons why this system has been extensively studied in the field of quantum chaos [8, 21, 24–27]. Moreover, this potential, which belongs to the C_{4v} symmetry group, is homogeneous, and then the classical trajectories exhibit mechanical similarity. That is, any trajectory $(x(t), y(t), p_x(t), p_y(t))$ run at a certain energy E can be scaled to $(x'(t), y'(t), p'_x(t), p'_y(t))$ at energy E' , by using the following scaling relations,

$$\begin{cases} x' := \eta x, & p'_x := \eta^2 p_x, \\ y' := \eta y, & p'_y := \eta^2 p_y, \\ t' := t/\eta, & S' = \eta^3 S, \end{cases} \quad (2)$$

where $\eta = \left(\frac{E'}{E}\right)^{1/4}$, and being S the corresponding classical action $S = \int_0^T (p_x \dot{x} + p_y \dot{y}) dt$.

B. Periodic orbits

PO trajectories for the quartic potential can be calculated by solving the system of differential equations

$$\begin{cases} \dot{x} = p_x, \\ \dot{y} = p_y, \\ \dot{p}_x = -(xy^2 + \epsilon x^3), \\ \dot{p}_y = -(x^2 y + \epsilon y^3), \\ \dot{S}_x = p_x \dot{x} = p_x^2, \\ \dot{S}_y = p_y \dot{y} = p_y^2, \end{cases} \quad (3)$$

where the appropriate initial conditions are chosen to obtain the desired PO. These can be obtained by taking into account the (high) symmetry of the system [28]. Notice that the last two equations are added to calculate the classical action, which is also needed in our calculations.

In Fig. 1, we show the four POs considered in this work, which correspond to the horizontal/vertical, quadruple-loop, horizontal/vertical bowtie, and square trajectories of our system, respectively.

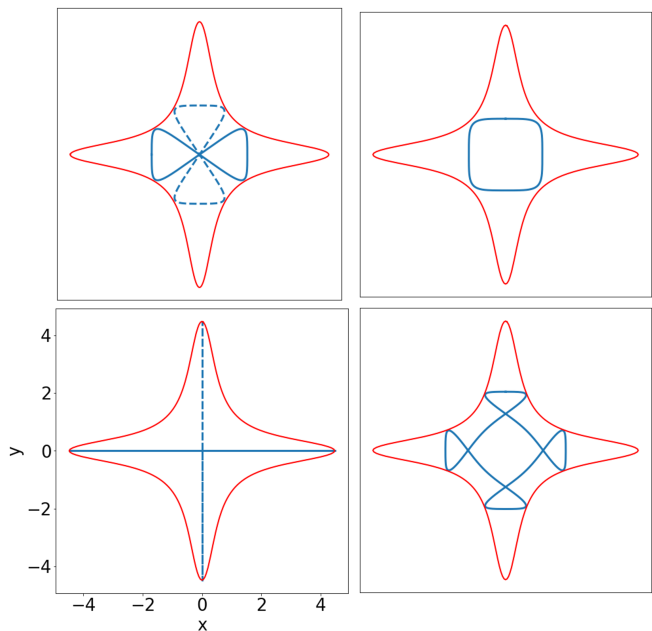


Figure 1. Trajectories corresponding to the four periodic orbits in blue (light gray): (from bottom left to upper right) horizontal/vertical, quadruple-loop, horizontal/vertical bowtie, and square, at $E = 1$. The corresponding equipotential is shown with the red (dark gray) line.

C. Quantum dynamics

The quantum dynamics of a system is obtained by solving the time-dependent Schrödinger equation,

$$i\hbar \frac{\partial \psi(x, y, t)}{\partial t} = \hat{H} \psi(x, y, t), \quad (4)$$

where \hat{H} is the associated Hamiltonian operator, which in our case was discussed in the previous Sect. II A. This partial differential equation can be integrated very efficiently using the fast Fourier transform (FFT) method developed by Kosloff and Kosloff [29]. With this method, an initial quantum state $\psi_0(x, y)$, with certain (mean) energy E_0 , can be propagated in time obtaining the corresponding time evolved state $\psi(x, y, t)$.

This constitutes the foundation of our computations, in which we will use the method described above to train the RC approach described in Sect. II G.

D. Eigenfunctions

From the time evolved $\psi(x, y, t)$ of a suitable initial quantum state $\psi_0(x, y)$ the eigenenergies and eigenfunctions of the quantum system with similar energies to E_0 can be calculated, by performing the following steps

1. Prepare an initial wavefunction $\psi_0(x, y)$ as a minimum uncertainty Gaussian wave packet with mean

energy E_0 .

$$\begin{aligned} \psi_0(x, y) = & \pi^{-1/8} e^{-(x-x_0)^2/(4\Delta x)^2} \\ & \times e^{-(y-y_0)^2/(4\Delta y)^2} \\ & \times e^{i(p_{x,0}x + p_{y,0}y)/\hbar}, \end{aligned} \quad (5)$$

where (x_0, y_0) is the central position, $\Delta x, \Delta y$ are the spread in the x and y directions, and $(p_{x,0}, p_{y,0})$ is the momentum of the wavepacket. The energy of the wavepacket in Eq. (5) corresponds to the value of the Hamiltonian function (1), at the central position (x_0, y_0) and momentum $(p_{x,0}, p_{y,0})$.

2. Compute the time evolution $\psi(x, y, t)$ under Hamiltonian $\hat{H}(x, y)$. For the first t_{train} time steps we use the FFT method proposed by Kosloff and Kosloff [29]. For the next t_{test} steps we use the RC algorithm proposed in Ref. [20] and summarized in Sect. II F below.
3. Calculate the energy spectrum $I(E)$. For this purpose, we first calculate the time-correlation function

$$\begin{aligned} C(t) = \langle \psi(t) | \psi(0) \rangle = & \quad (6) \\ \int_{(x,y)} \psi(x, y, t)^* \psi_0(x, y) dx dy. & \end{aligned}$$

Then, we obtain the energy spectrum $I(E)$ as the Fourier transform of the time-correlation function

$$I(E) = \int_t C(t) e^{-iEt/\hbar} dt, \quad (7)$$

where the integral should be done for infinite time. For practical purposes, however, the integral is done for a large interval of time $[0, T]$. The eigenenergies E_n correspond to the peaks of the energy spectrum function $|I(E)|$.

4. Calculate the eigenfunctions $\phi_n(x, y)$ by performing the Fourier transform of $\psi(x, y, t)$ at the eigenenergies E_n

$$\phi_n(x, y) = \int_t \psi(x, y, t) e^{iE_n t/\hbar} dt. \quad (8)$$

Therefore, the problem is reduced to propagating an initial wavepacket in time by solving the time-dependent Schrödinger equation (in step 2) using RC.

In this work, we calculate the eigenfunctions and eigenenergies with A_1 symmetry, i.e. most symmetric, for three different initial conditions at energies $E_0 = 1, 10$ and 100, respectively. For simplicity of visualization, all the systems are scaled to energy $E = 1$ using the scaling relations in Eq. (2). The parameters of the initial wavepackets are reported in Table I.

E	x_0	y_0	Δx	Δy	p_0	t_{train}	t_{test}	Δt
1	0	0	0.5	0.5	1	1500	4650	0.00140
10	1.860	1.860	$2^{-1/2}$	$2^{-1/2}$	-2	3000	10000	0.00030
100	3.665	3.665	1	1	-3	5000	8000	0.00003

Table I. Parameters of the initial wavefunctions, as described in Eq. (16) at three different energies used in our calculations. Training and test time for the RC algorithm, and time intervals between steps are also given in the last three columns.

At this point, two somewhat related issue should be considered: symmetry and propagation time. Regarding the former, notice that the symmetry of the initial wavepacket determines the set of eigenfunctions obtained with this method. That is, if the initial wavepacket in Eq. (5) has a certain symmetry (for example along the x axis), the resulting wavefunctions will also have this same symmetry. Accordingly, if the whole set of eigenfunctions in a given energy interval wants to be collected, the previous steps need to be repeated with different symmetry-adapted $\psi_0(x, y)$'s taking into account all possible symmetries in the system. Regarding the latter, consider that among that the eigenvalues resolution of our calculated is mainly dictated by the propagation time of the initial wavepacket. In the ideal case of an infinite time span, all eigenvalues would be resolved no matter how close they would be. However, this is not feasible in an actual numerical calculation, and then the propagation time has to be selected taking into account the density of states of the system. Fortunately, this function function can be semiclassically ascertained. The leading term in the corresponding expansion in \hbar^{-1} is obtained by deriving the Weyl formulae, and higher order terms can also be added in the expansion, for example to account for the effect of the parity in the eigenfunctions existing along the different symmetry lines. This is mandatory in our case of the quartic oscillator, due to the high symmetry of the potential. Full details and explicit expressions for the quartic potential in our work can be found in Refs. [28, 30].

Moreover, also note that the parameter t_{train} is influenced by the system initial energy, with higher energies requiring more training steps for the reservoir to effectively learn the system dynamics. As system complexity rises with energy, enlarging t_{train} becomes necessary due to the increased challenge for the reservoir to capture intricate dynamics. Proper training allows the reservoir to autonomously predict future system dynamics. Consequently, a smaller t_{train} could compromise the capacity of generalization of the method. Increasing t_{train} to the values in Table I ensures a correct training, reducing the risk of overfitting to the training dynamics.

Scar	T	ND	P	n	μ	$(x_0, y_0, p_{x_0}, p_{y_0})$
Horizontal/vertical	33.17	0	0	12,14,16,18,20,22, 42,47,53, 58,62	16	$(0, 0, \sqrt{2}, \sqrt{2})$
Quadruple-loop	18.75	0	4	4,5,6,7,8,9,10	12	$(0, 2.028, 1.384, 0)$
Bowtie hor/ver	9.54	0	2	20,22,24	4	$(0, 1.655, 1.401, 0)$
Square	7.84	0	4	3,4,5,6,7,8	4	$(0, 1.239, 1.410, 0)$

Table II. Number of Dirichlet conditions on the wave functions at symmetry lines (ND), ratio between the period of the full periodic orbit and that of the desymmetrized periodic orbit (P), excitation number (n), Maslov index (μ) and initial conditions for the four periodic orbits studied in this work, at energy $E = 1$. The values of all the parameters are taken from Ref. [28].

E. Scar functions

Apart from the eigenfunctions, we also use the RC algorithm to compute the scarred functions discussed in Sect. I along different POs, and for different energy ranges. For this purpose, we use the method introduced in Ref. [8], that can be summarized as follows:

1. Select a PO of the system.
2. Prepare an initial *tube* wavefunction $\psi_0^{\text{tube}}(x, y)$, localized on a tube along the PO, given by [8]

$$\psi_0^{\text{tube}}(x, y) = \int_0^T e^{i\epsilon_n t/\hbar} \psi^{\text{FG}}(x, y, t) dt, \quad (9)$$

where T is the period of the periodic orbit, and ϵ_n is the associated Bohr-Sommerfeld (BS) quantized energy (see details below). The function $\psi^{\text{FG}}(x, y, t)$ is a frozen Gaussian [31] centered on the PO trajectory, so that its probability density is forced to stay around such PO

$$\psi^{\text{FG}}(x, y, t) = e^{-\alpha_x(x-x_t)^2 - \alpha_y(y-y_t)^2} \cdot e^{i[p_{x_t}(x-x_t) + p_{y_t}(y-y_t) + \theta_t]/\hbar}, \quad (10)$$

where $(x_t, y_t, p_{x_t}, p_{y_t})$ is the trajectory of the PO, and α_x and α_y are the widths along the two spatial dimensions. In our case, we set $\alpha_x = \alpha_y = 1$. The term θ_t is a phase defined as

$$\theta_t = \frac{S(t)}{\hbar} - \mu \frac{\pi}{2} \quad (11)$$

where μ is the Maslov index [32], ensuring that the wavefunction fulfils a constructive interference along the PO. The corresponding BS energies are computed by imposing that

$$\theta(T) = \frac{S(T)}{\hbar} - \frac{\mu\pi}{2} = 2\pi n \quad (12)$$

Using Eqs. (12) and (2) it is found that

$$\epsilon_n = \left[\frac{2\pi\hbar}{S_0} \left(P \cdot n + \frac{\mu}{4} + \frac{P \cdot ND}{2} \right) \right]^{4/3}, \quad (13)$$

where ND is the number of Dirichlet conditions on the wave functions at the symmetry lines (axis and

diagonals), P is the ratio between the period of the full PO and that of the desymmetrized PO (that is, reduced to the fundamental domain), and n is the excitation number. The values of these coefficients for the cases considered in this work are shown in Table II.

3. Compute the time evolution $\psi(x, y, t)$ under the Hamiltonian $\hat{H}(x, y)$. Again, we use the FFT method to train a RC model and use it to further propagate the wavefunction.
4. Calculate the low-resolution energy spectrum $I(E)$. First, we calculate the time-correlation function in Eq. (7). Then, we obtain the energy spectrum $I(E)$ as the Fourier transform of the time-correlation function

$$I(E) = \int_{-t_E}^{t_E} C(t) e^{-iEt/\hbar} dt, \quad (14)$$

evaluated for a short period of time t_E , taken as the Ehrenfest time

$$t_E = \frac{1}{2\lambda} \ln \left(\frac{\mathcal{A}}{\hbar} \right). \quad (15)$$

In the case of our quartic potential $\lambda \approx 0.385E^{1/4}$ is the Lyapunov exponent of the system and $\mathcal{A} = 11.1E^{3/4}$ is the area of a characteristic Poincaré surface of section [25]. The peaks in this low-resolution spectrum E_n will be used to compute the scarred functions.

5. Calculate the scarred functions $\psi^{\text{scar}}(x, y)$ by performing the Fourier transform of $\psi(x, y, t)$ at the energies E_n

$$\psi_n^{\text{scar}}(x, y) = \int_{-t_E}^{t_E} \psi(x, y, t) e^{iE_n t/\hbar} dt. \quad (16)$$

F. Reservoir computing

RC is a machine learning method that has proven very useful in predicting the evolution of time series. In the

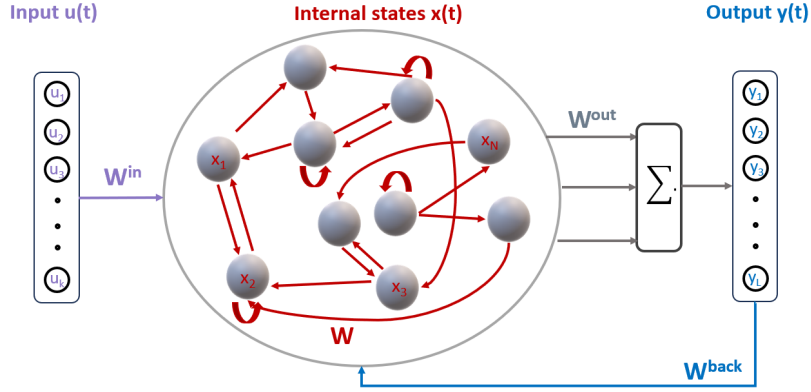


Figure 2. Architecture of a RC model. Only the readout layer W^{out} is learnt during training.

RC framework, the learning complexity of the algorithm is reduced to performing a linear regression. This machine learning algorithm consists of a neural network, where each of its nodes evolves in time with a dynamics that depends on the input-output dynamics. For this reason, the internal states of the network are called *echo states*, since they can be thought of as an echo of their past [33]. Then, a linear model is fit to find the relationship between the evolution of the internal states of the network and the actual dynamics of the system we aim to predict. The structure of the RC algorithm is schematically shown in Fig. 2, where

- $W^{\text{in}} \in M(\mathbb{R})_{N \times K}$ gives the weights from the input units to the internal states,
- $W \in M(\mathbb{R})_{N \times N}$ gives the weights between the different internal states,
- $W^{\text{out}} \in M(\mathbb{R})_{L \times N}$ gives the weights from internal states to output units, and
- $W^{\text{back}} \in M(\mathbb{R})_{N \times L}$ gives the weights from the output units to the internal states,

and where

- $\vec{u}(t) = (u_1(t), u_2(t), \dots, u_K(t))$ is a K -dimensional vector giving the input units at time t ,
- $\vec{x}(t) = (x_1(t), x_2(t), \dots, x_N(t))$ is an N -dimensional vector giving the internal states at time t , and
- $\vec{y}(t) = (y_1(t), y_2(t), \dots, y_L(t))$ is an L -dimensional vector giving the output units at time t .

Notice that the matrices W^{in} , W and W^{back} are randomly chosen before the training phase so that they do not change during training. The only learnable parameters are the weights W^{out} . The steps to train the RC algorithm are the following:

1. Generate the reservoir matrices $(W, W^{\text{in}}, W^{\text{back}})$ randomly.

2. Update the internal states by teacher forcing:

$$\begin{aligned} \tilde{x}(t) &= f(W^{\text{in}}u(t) + Wx(t-1) + W^{\text{back}}y_{\text{teach}}(t-1)) \\ x(t) &= (1-\alpha)x(t-1) + \alpha\tilde{x}(t) \end{aligned} \quad (17)$$

where y_{teach} is the output that we want our network to predict, $\alpha \in (0, 1]$ is the leaking rate and f is the activation function. Usually, $f(\cdot) = \tanh(\cdot)$, which is applied component-wise.

3. Discard a transient of t_{min} states to guarantee the convergence of the reservoir dynamics.
4. Find the readout matrix W^{out} by minimizing the mean squared error with L^2 regularization (ridge regression):

$$\text{MSE}_r(y, y_{\text{teach}}) = \frac{1}{T - t_{\text{min}}} \sum_{t=t_{\text{min}}}^T \left(y_{\text{teach}}(t) - W^{\text{out}}x(t) \right)^2 + \gamma \|W^{\text{out}}\|^2, \quad (18)$$

Notice that this step only requires performing a linear regression.

The steps to make the predictions after training the network are the following:

1. Given an input $u(t)$, update the state of the reservoir:

$$\begin{aligned} \tilde{x}(t) &= f[(W^{\text{in}}u(t) + Wx(t-1) + W^{\text{back}}y(t-1))] \\ x(t) &= (1-\alpha)x(t-1) + \alpha\tilde{x}(t) \end{aligned} \quad (19)$$

where $y(t-1)$ is the prediction of the output at time $t-1$.

2. Compute the prediction $y(t)$:

$$y(t) = W^{\text{out}}x(t). \quad (20)$$

In our setting, the RC model is used without the input layer since we aim to propagate a dynamical system without using any explanatory variables. In this case, the term $W^{\text{in}}u(t)$ is removed from Eqs. (17) and (20).

G. Reservoir computing for quantum systems

The propagation of the initial wavepacket is done by training a RC model with the wavefunctions calculated by the FFT method until time t_{train} and then using the RC model to predict the evolution until time $t_{\text{train}} + t_{\text{test}}$. In the RC framework, $\psi(x, y, t)$ can be represented as a set of matrices $\{\psi(x, y, t)\}_t$, where each matrix contains the values of $\psi(x, y)$ at time t in a grid of points spanning (x, y) . However, in Ref. [20] we proposed a more efficient method to adapt RC to propagate quantum systems.

Two main challenges need to be overcome to adapt the traditional RC to propagate wavefunctions

- **Complex numbers:** In the usual RC framework all the vectors and matrices are real-valued. However, the target time series for this quantum problem is a wavefunction $\psi(x, y, t)$ which, in general, takes complex values. We adapted the RC algorithm to work with complex numbers by proposing the activation function

$$f(x) = \tanh(\text{Re}(x)) + i \tanh(\text{Im}(x)) \quad (21)$$

and providing a closed-form solution for the complex-valued ridge regression

$$W^{\text{out}} = (X^* X + \alpha \mathbb{I})^{-1} \times (X^* f_{\text{out}}^{-1}(\vec{y}_{\text{teach}})), \quad (22)$$

where $*$ denotes the conjugate transpose, and X is the matrix containing the internal states.

- **High-dimensional data:** The target data is represented as a matrix, where each entry is the value of the wavefunction in a discretized spatial grid. The size of this matrix increases exponentially with the dimension of the physical system, that is, the dimension of (x, y) . With large input sizes we need to use large reservoirs W . If the complexity of the neural network is too large, the linear model can easily overfit the training data, and therefore be unable to predict the evolution of the dynamical system. For this reason, we proposed a new training strategy that reduces the overfitting of the algorithm. This learning strategy shows the reservoir how small predicting errors modify the internal states during the test phase. This reduces overfitting, decreasing the test error significantly. For further information on this method, refer to Ref. [20].

Table III shows the training parameters used for each of the systems studied in this work. For all systems we used $f^{\text{out}} = \mathbb{I}$ and $t_{\text{min}} = 500$. For the multi-step process described in Ref. [20], we used 80% of the training data for the first training step and 20% for the second step. The spectral radius of the internal states W is set $\rho(W) = 0.5$, and the density of W is set to 0.005. Even though a cumbersome machine learning model such

Calculation	α	γ	N
Eigenfunctions $E = 1$	0.2	0.001	2000
Eigenfunctions $E = 10$	0.2	0.001	2000
Eigenfunctions $E = 100$	0.017	0.1	10000
Horizontal/vertical scar	0.1	1.0	1500
Quadruple-loop scar	0.3	0.1	2000
Bowtie hor/ver scar	0.3	0.1	3000
Square scar	0.3	0.1	3000

Table III. Reservoir computing training parameters, as defined in Sect. IIF, used in the calculation of different eigenfunctions and scars for the quartic potential in Eq. (1).

as Bayesian optimization could have been used to select the hyperparameters, we consider that, in this case, such methods are not necessary. We follow instead the criteria given in Ref. [34] to choose the appropriate training parameters.

III. RESULTS

In this section, we use our RC method to calculate eigenfunctions and scarred functions of the coupled quartic oscillator (1), and examine its performance for these two tasks. Let us start with the calculation of eigenfunctions.

First, we compute the quantum dynamics generated by three different initial wavepackets at $E_0 = 1, 10$ and 100 , respectively, and the parameters reported in Table I, and from them we compute the corresponding spectra and eigenstates, with the method described in Sect. II.

In the left panel of Fig. 3 we present, as an example, the spectrum for the $E_0 = 10$ case. The packet is launched along the main diagonal, and accordingly, only totally symmetric eigenstates, i.e. belonging to the A_1 symmetry class, are generated. As can be seen, four con-

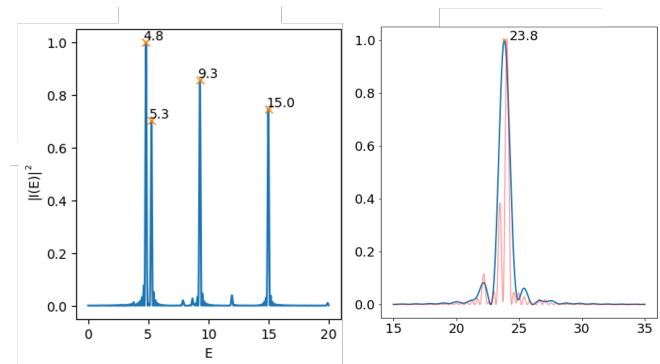


Figure 3. (Left) Example of the modulus of the energy spectrum $|I(E)|^2$ for the system at $E = 10$. (Right) Long time energy spectrum $|I(E)|^2$, in red (light gray), and its low-resolution version, in blue (dark gray), for the quadruple-loop scar function at energy $E = 22.824$.

E_0	E_n	E_n MSE	ϕ_n MSE
1	.56323	$4 \cdot 10^{-10}$	$5 \cdot 10^{-7}$
	1.8848	$< 10^{-10}$	$4 \cdot 10^{-7}$
	2.8638	$4 \cdot 10^{-10}$	$1 \cdot 10^{-5}$
10	4.8286	$1 \cdot 10^{-8}$	$6 \cdot 10^{-6}$
	5.2584	$1 \cdot 10^{-8}$	$7 \cdot 10^{-6}$
	9.3067	$1 \cdot 10^{-8}$	$9 \cdot 10^{-6}$
	14.9547	$1 \cdot 10^{-8}$	$1 \cdot 10^{-5}$
100	28.6843	$4 \cdot 10^{-8}$	$8 \cdot 10^{-6}$
	46.8794	$1 \cdot 10^{-6}$	$2 \cdot 10^{-5}$
	48.5846	$6 \cdot 10^{-6}$	$3 \cdot 10^{-6}$
	50.2605	$6 \cdot 10^{-7}$	$8 \cdot 10^{-7}$
	52.5642	$3 \cdot 10^{-5}$	$4 \cdot 10^{-6}$
	56.9221	$3 \cdot 10^{-6}$	$5 \cdot 10^{-7}$
	83.1969	$1 \cdot 10^{-5}$	$6 \cdot 10^{-7}$
	87.9381	$9 \cdot 10^{-8}$	$6 \cdot 10^{-7}$
	89.3304	$2 \cdot 10^{-5}$	$9 \cdot 10^{-6}$

Table IV. Eigenenergies E_n for the different eigenfunctions ϕ_n shown in Figs. 4, 5, and 6, together with the corresponding mean squared errors calculated by comparison with the ‘exact’ variational ones, obtained from the three initial wavepackets specified in Table I.

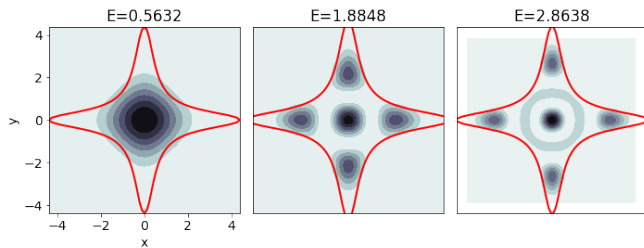


Figure 4. Probability density of the eigenfunctions of the coupled quartic oscillator obtained from propagating an initial wavepacket with energy $E = 1$. The red (light grey) solid lines depict the equipotential curves.

spicuous peaks, at the eigenenergies reported in Table IV, are clearly observed.

The associated eigenfunctions are shown in Figs. 4, 5 and 6, respectively. For comparison, we have also calculated the eigenenergies and eigenfunctions using the variational method [35], which will be considered to be the *exact* ones, in contrast to the *predicted* ones produced with RC. As can be seen the first three A_1 eigenstates (see Fig. 4) corresponds, as expected, to states $(n_x, n_y) = (0, 0), (1, 1),$ and $(2, 2)$, respectively. In the next two figures, we show more excited eigenfunctions, which then exhibit more complicated nodal pattern topologies. Interesting to note that some very excited cases, in particular those for $E_n = 50.2597, 83.2003$ and 89.3349 in Fig. 6, appear as clear scars in the original sense of Heller [4] of the double-loop and diagonal POs.

The mean squared error (MSE) of the predicted

System	Method	Execution time (in hours)
Eigenfunctions $E = 1$	FFT	3:35
	RC	0:10
Eigenfunctions $E = 10$	FFT	4:50
	RC	0:36
Eigenfunctions $E = 100$	FFT	24:47
	RC	1:34
Horizontal/vertical scar	FFT	2:58
	RC	0:12
Quadruple-loop scar	FFT	1:32
	RC	0:07
Bowtie hor/ver scar	FFT	3:27
	RC	0:24
Square scar	FFT	3:44
	RC	0:25

Table V. Execution times for the Fast Fourier Transform integrator [29] and the RC model, for all cases studied in this work.

eigenenergies and eigenfunctions, compared to the exact ones, are provided in Table IV. As can be seen, the MSE of the eigenenergies increases with the energy of the system, since the eigenfunctions become more complex and thus harder for the RC algorithm to predict its time evolution. However, the MSE of all the energies and eigenfunctions is of the order or smaller than 1×10^{-5} , which means that the machine learning RC model can correctly propagate in time the quantum states of this chaotic system. Therefore, the RC algorithm, being agnostic to the underlying physical model of the system, can reproduce the dynamics of complex quantum chaotic

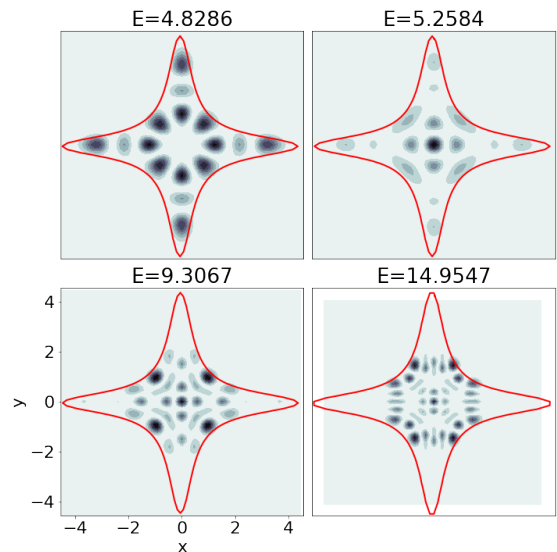


Figure 5. Same as Fig. 4 for $E = 10$, scaled to the domain corresponding to $E = 1$.

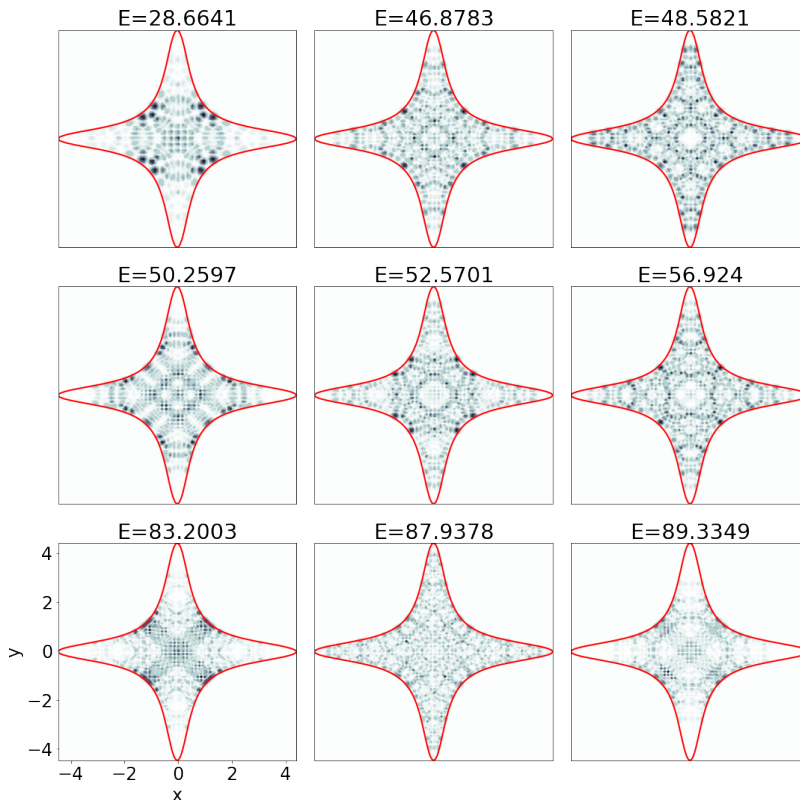


Figure 6. Same as Fig. 5 for $E = 100$.

systems, which proves the versatility of the algorithm to be adapted to multiple quantum systems [20].

The advantage of using a machine learning algorithm instead of a classical numerical integrator is the execution time needed to propagate the initial state in time. Table V shows the execution time for the FFT integrator and the RC models. These results show that the RC method is much faster than the classical integrator, which makes it suitable for predicting the long-time evolution of quantum states.

Apart from the eigenfunctions, we have also used RC to calculate some scarred functions at different energies for the four POs shown in Fig. 1. Notice that the horizontal/vertical and bowtie horizontal/vertical POs are in fact made of two POs (solid and dashed lines in Fig. 1) to take into account the symmetry of Hamiltonian (1). Similarly to what was done in the case of the eigenstates, this choice is made so that the resulting scarred functions belong to the A_1 irreducible representation, that is, they are symmetric with respect to the x , y axis, and the two diagonals $y = \pm x$.

As explained in Sect. II E, the energies of the scarred functions are obtained by finding the peaks of the low-resolution energy spectrum generated from a wavepacket launched along the selected PO. An example of the corresponding high (in red) and low-resolution, resolved up to the Ehrenfest time, (in blue) spectra for the quadruple-loop PO at $E = 22.824$ are shown in the right panel of

Fig. 3. As can be seen, for the longer time the energy peaks in the spectrum are more pronounced and better resolved, while the low-resolution spectrum has wider peaks which contain several high-resolution peaks. This is an effect due to the inclusion or not of dynamical information beyond the first recurrence along the PO, and was thoroughly discussed in Refs. [36, 37].

Once the energies of the scar functions have been calculated, the associated scarred functions are obtained with the procedure described in Sect. II E. Figures 7, 8, 9, and 10 show some scarred functions calculated for the four POs in Fig. 1 at different energies (scaled to energy $E = 1$ for an easier visualization). We see that all the scarred functions appear very well localized around their associated PO, showing an increasing consecutive excitation as energy increases. Actually, in almost all cases scar quantum numbers can be easily assigned, being this specially clear in all panels of Figs. 7 and 8. On the other hand, in some cases an 'interaction' between POs is apparent. For example, the scarred function shown in Fig. 10 for $E = 15.78$ is mainly localized around the square PO, but it also has visible and easily countable nodes along the quadruple-loop PO. This is because the time-propagation of the initial wavefunction gathers information about the phase space around both POs, which then shows in the resulting scar. Moreover, notice that in Fig. 8, there is a quadruple-loop scar function at a similar energy, i.e. $E = 14.693$, to that of the square

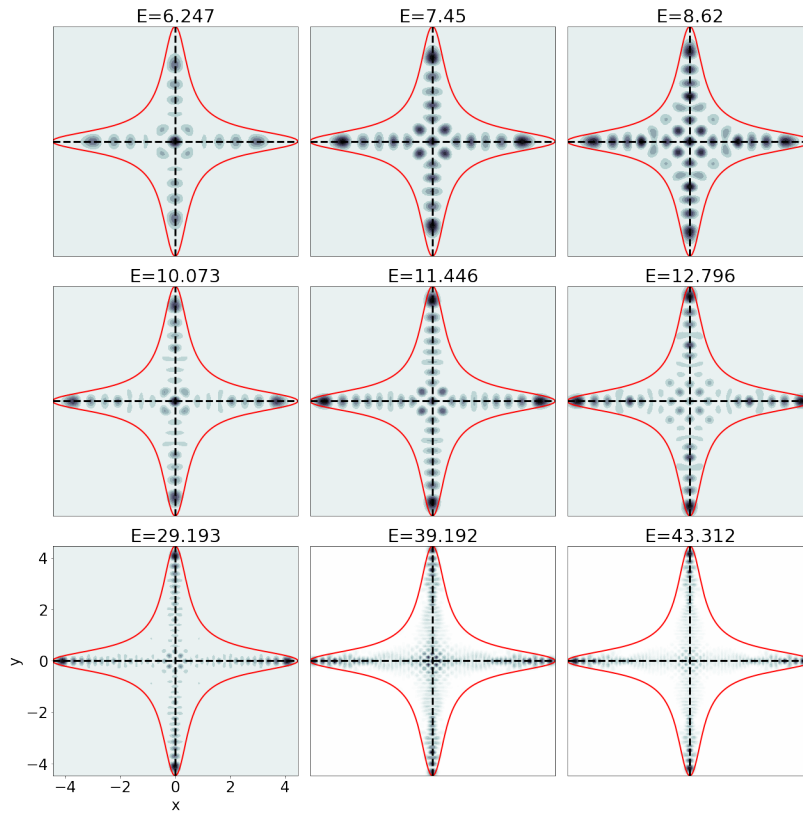


Figure 7. Probability density of the scar function for the horizontal/vertical periodic orbit, at different energies (see Table II). The solid red (light gray) lines depict the equipotential curves, while the dashed black lines illustrate the periodic orbits

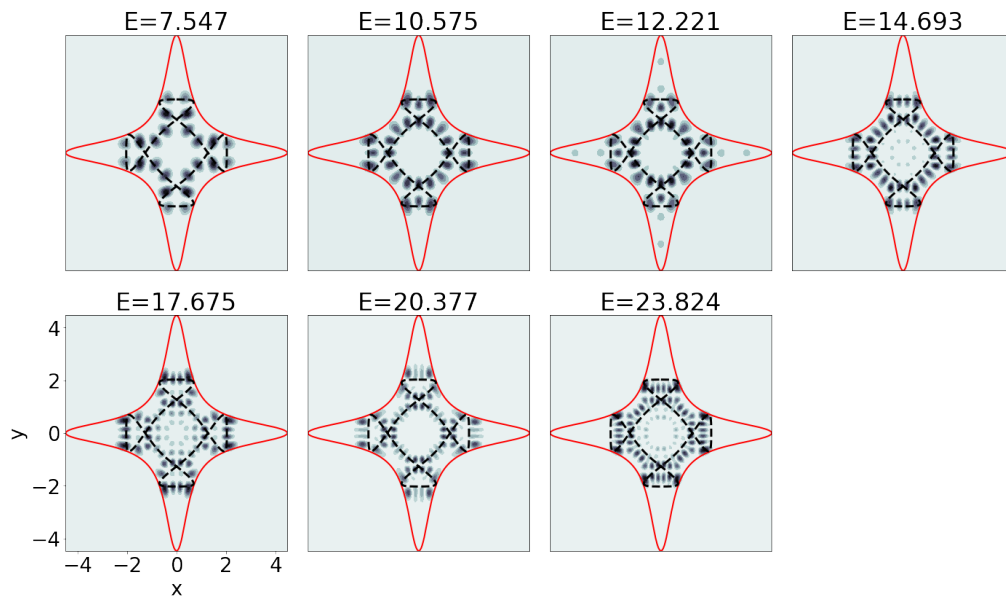


Figure 8. Same as Fig. 7 for the quadruple-loop periodic orbit.

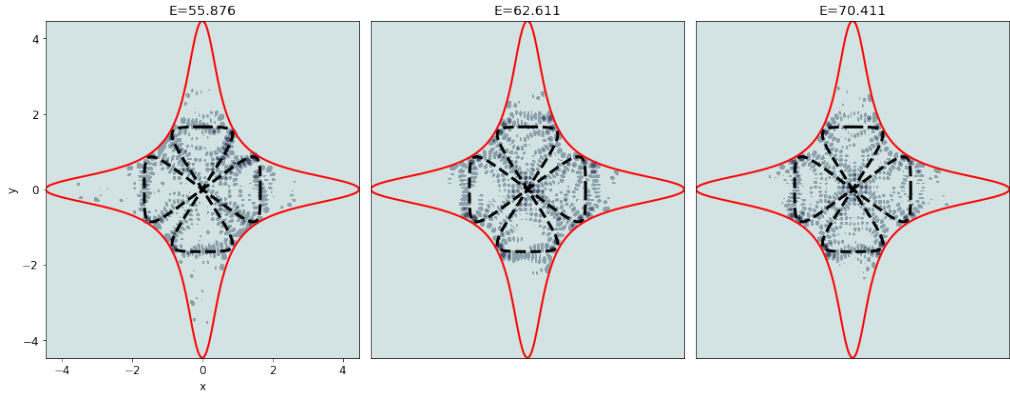


Figure 9. Same as Fig. 7 for the bowtie periodic orbit.

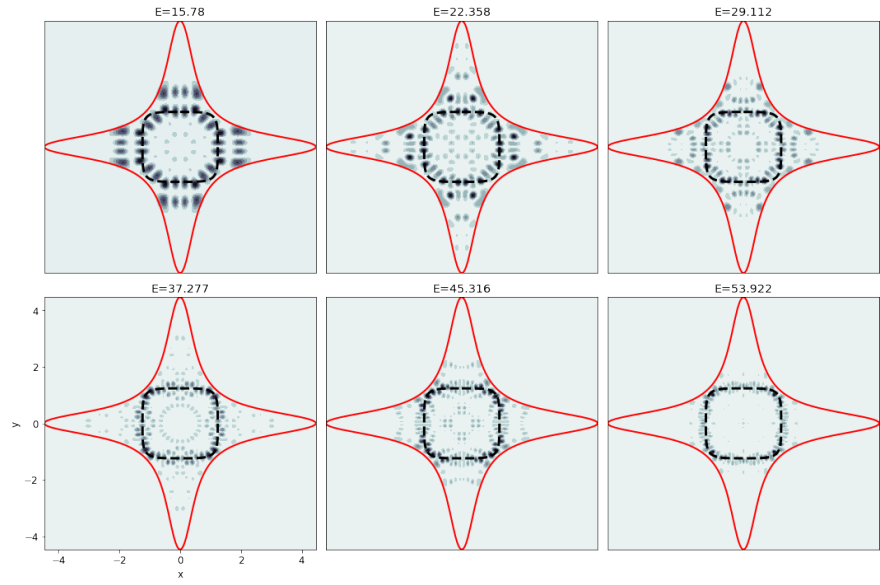


Figure 10. Same as Fig. 7 for the square periodic orbit.

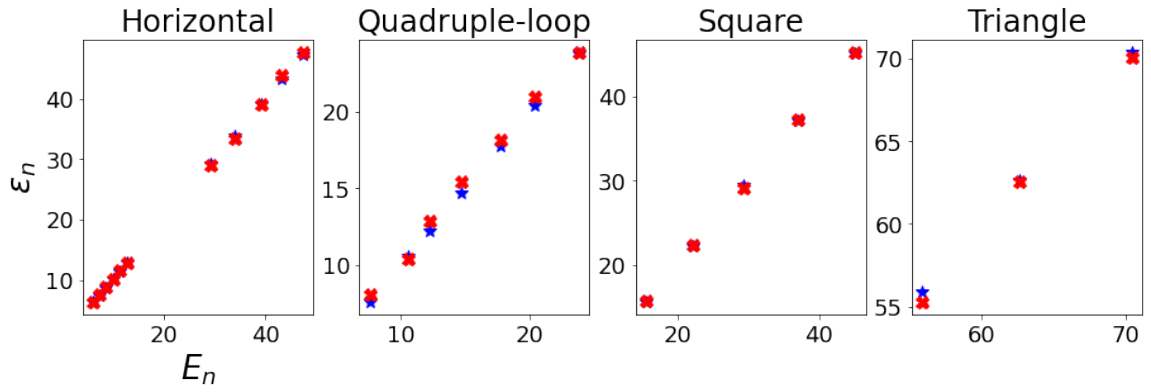


Figure 11. Comparison of the semiclassical energies (red crosses) with the scar energies obtained with the reservoir computing approach (blue stars).

scarred function mentioned before, which is an indication of the possibility of interaction between them. On the other hand, other scarred functions appear totally localized around one single PO (see, for example, the horizontal scarred functions in Fig. 7, or the square scarred function at $E = 53.922$ in Fig. 10). Again, a complete discussion of this effect can be found in Refs. [36, 37].

To end this subsection, we compare the energies obtained by our RC method with the Bohr-Sommerfeld quantized energies. The result is shown in Fig. 11. As can be seen, the energies obtained with both methods are very similar. Some small differences between the Bohr-Sommerfeld energies and the quantum energies obtained with the RC method may, however, be expected. First, the Bohr-Sommerfeld energies are a semiclassical approximation of the true quantum energies, which include all quantum effects. Second, the Bohr-Sommerfeld approximation only takes into account the influence of a single PO for each scarred state, and we have already discussed that some of the resulting scarred functions obtained with the RC method are the result of (small) interactions between different POs, which also causes small differences in the obtained energies.

In conclusion, our results show that the RC method is able to predict the time evolution of the coupled quartic oscillator for different initial conditions, and obtain, with high accuracy, the associated eigenenergies, eigenfunctions and scarred functions. This efficient machine learning algorithm is faster than the traditional PDE solver, and it is easily adaptable to different systems.

IV. CONCLUSIONS

In this paper, we introduced a machine learning method to efficiently calculate the eigenstates and scarred functions of quantum systems. In particular, the novel algorithm called RC, which has been shown to excel at predicting the evolution of chaotic time series [38, 39], is used. As an illustration, this algorithm has been applied to the coupled quartic oscillator, which has been extensively studied in the field of quantum chaos.

From a suitable initial wavepacket, we have used RC to propagate the quantum state in time. Then, by performing a Fourier transform we have been able to recover the eigenstates and eigenenergies of the system at different energies in the vicinity of the mean energy of the packet. Moreover, given an initial condition localised around a PO, we have calculated the associated scarred functions at multiple energies by computing the low-resolution spectrum, for four different POs of the quartic oscillator. The possibility of performing extensive calculations involving many excited scarred states is of importance in the field of quantum chaos [12–14].

The results have been compared with more traditional methods, such as the variational method and the Bohr-Sommerfeld semiclassical quantization. We have seen that even with high energies and complex wavefunction, the RC algorithm can reproduce the eigenstates and scarred functions with high accuracy, meaning that the method can correctly propagate the initial wavefunction in time. Moreover, the simple training strategy of RC provides fast execution times when compared to the other classical methods. Finally, as we have shown in a previous work [20], RC is easily adaptable to propagate different systems, which makes the method very versatile.

CODE AVAILABILITY

The code and data that support the findings of this study are openly available in https://github.com/laiadc/Scars_RC.

ACKNOWLEDGMENTS

The project that gave rise to these results received the support of a fellowship from "la Caixa" Foundation (ID 100010434). The fellowship code is LCF/BQ/DR20/11790028. This work has also been partially supported by the Spanish Ministry of Science, Innovation and Universities, Gobierno de España, under Contract No. PID2021-122711NB-C21.

-
- [1] M. C. Gutzwiller, *Chaos in Classical and Quantum Mechanics* (Springer-Verlag, New York, 1990).
 - [2] M. V. Berry, Quantum scars of classical closed orbits in phase space, *Proceedings of the Royal Society of London. A. Mathematical and Physical Sciences* **423**, 219 (1989).
 - [3] O. Bohigas, M. J. Giannoni, and C. Schmit, Characterization of chaotic quantum spectra and universality of level fluctuation laws, *Phys. Rev. Lett.* **52**, 1 (1984).
 - [4] E. J. Heller, Bound-state eigenfunctions of classically chaotic hamiltonian systems: Scars of periodic orbits, *Phys. Rev. Lett.* **53**, 1515 (1984).
 - [5] L. Kaplan and E. Heller, Linear and nonlinear theory of eigenfunction scars, *Ann. Phys.* **264**, 171 (1998).
 - [6] G. G. de Polavieja, F. Borondo, and R. M. Benito, Scars in groups of eigenstates in a classically chaotic system, *Phys. Rev. Lett.* **73**, 1613 (1994).
 - [7] E. G. Vergini and G. G. Carlo, Semiclassical construction of resonances with hyperbolic structure: the scar function, *J. Phys. A: Mathematical and General* **34**, 4525 (2001).
 - [8] F. Revuelta, R. Benito, F. Borondo, and E. Vergini, Using basis sets of scar functions, *Phys. Rev. E* **87**, 042921 (2013).
 - [9] A. Goussev, R. A. Jalabert, H. M. Pastawski, and D. A. Wisniacki, Loschmidt echo, *Scholarpedia* **7**, 11687 (2012).

- [10] P. D. Bergamasco, G. G. Carlo, and A. M. Rivas, Relevant out-of-time-order correlator operators: Footprints of the classical dynamics, *Phys. Rev. E* **102**, 052133 (2020).
- [11] E. Ravinovici, A. Sánchez-Garrido, R. Shir, and J. Sonner, Operator complexity: a journey to the edge of krylov space, *J. High Energy Phys* **2021**, 62 (2021).
- [12] D. A. Wisniacki, E. Vergini, R. M. Benito, and F. Borondo, Signatures of homoclinic motion in quantum chaos, *Phys. Rev. Lett.* **94**, 054101 (2005).
- [13] D. A. Wisniacki, E. Vergini, R. M. Benito, and F. Borondo, Scarring by homoclinic and heteroclinic orbits, *Phys. Rev. Lett.* **97**, 094101 (2006).
- [14] Q. Hummel, K. Richter, and P. Schlagheck, Genuine many-body quantum scars along unstable modes in Bose-Hubbard systems, *Phys. Rev. Lett.* **130**, 250402 (2023).
- [15] D. E. Rumelhart, G. E. Hinton, and R. J. Williams, Learning internal representations by error propagation, in *Parallel Distributed Processing: Explorations in the Microstructure of Cognition, Volume 1: Foundations* (MIT Press, Cambridge, MA, 1986) pp. 318–362.
- [16] S. Hochreiter and J. Schmidhuber, Long short-term memory, *Neural Comput.* **9**, 1735 (1997).
- [17] J. Pathak, Z. Lu, B. Hunt, M. Girvan, and E. Ott, Using machine learning to replicate chaotic attractors and calculate Lyapunov exponents from data, *Chaos* **27**, 121102 (2017).
- [18] J. Pathak, B. Hunt, M. Girvan, Z. Lu, and E. Ott, Model-free prediction of large spatiotemporally chaotic systems from data: A reservoir computing approach, *Phys. Rev. Lett.* **120**, 024102 (2018).
- [19] L. Domingo, M. Grande, F. Borondo, and J. Borondo, Anticipating food price crises by reservoir computing, *Chaos, Solitons and Fractals* **174**, 113854 (2023).
- [20] L. Domingo, J. Borondo, and F. Borondo, Adapting reservoir computing to solve the schrödinger equation, *Chaos* **32**, 063111 (2022).
- [21] F. Revuelta, E. Vergini, R. Benito, and F. Borondo, Computationally efficient method to construct scar functions, *Phys. Rev. E* **85**, 026214 (2012).
- [22] P. Dahlqvist and G. Russberg, Existence of stable orbits in the x^2y^2 potential, *Phys. Rev. Lett.* **65**, 2837 (1990).
- [23] J. Zuñiga, A. Bastida, and A. Requena, Quantum dynamics of oblique vibrational states in the Hénon-Heiles system, *J. Phys. Chem. A* **127**, 8663 (2023).
- [24] O. Bohigas, S. Tomsovic, and D. Ullmo, Manifestations of classical phase space structures in quantum mechanics, *Phys. Rep.* **223**, 43 (1993).
- [25] F. Revuelta, E. Vergini, R. M. Benito, and F. Borondo, Short-periodic-orbit method for excited chaotic eigenfunctions, *Phys. Rev. E* **102**, 042210 (2020).
- [26] R. L. Waterland, J.-M. Yuan, C. C. Martens, R. E. Gillilan, and W. P. Reinhardt, Classical-quantum correspondence in the presence of global chaos, *Phys. Rev. Lett.* **61**, 2733 (1988).
- [27] B. Eckhardt, G. Hose, and E. Pollak, Quantum mechanics of a classically chaotic system: Observations on scars, periodic orbits, and vibrational adiabaticity, *Phys. Rev. A* **39**, 3776 (1989).
- [28] F. Revuelta, *Estudio de la estructura de autofunciones de sistemas caóticos en una base de funciones de scar*, PhD Thesis, Universidad Politécnica de Madrid (2012), available at <https://oa.upm.es/10889/>.
- [29] D. Kosloff and R. Kosloff, A Fourier method solution for the time dependent Schrödinger equation as a tool in molecular dynamics, *J. Comput. Phys.* **52**, 35 (1983).
- [30] F. Revuelta, E. Vergini, R. M. Benito, and F. Borondo, Calculation of highly excited degenerate eigenstates of a chaotic system in energy windows, *Discontinuity Nonlinearity Complex.* **13**, 49 (2024).
- [31] J. Lu and X. Yang, Frozen gaussian approximation for high frequency wave propagation, *Commun. Math. Sci.* **9**, 663 (2011).
- [32] V. P. Maslov and M. V. Fedoriuk, *Semi-classical approximation in quantum mechanics*, Mathematical Physics and Applied Mathematics (Springer Dordrecht, Dordrecht Holland, 1981).
- [33] H. Jaeger, The "echo state" approach to analysing and training recurrent neural networks-with an erratum note, German National Research Center for Information Technology GMD Technical Report **148**, 09114 (2001).
- [34] M. Lukoševičius, A practical guide to applying echo state networks, in *Neural Networks: Tricks of the Trade: Second Edition*, edited by G. Montavon, G. B. Orr, and K.-R. Müller (Springer, Berlin, Heidelberg, 2012) pp. 659–686.
- [35] J. W. S. Rayleigh and E. Schrödinger, The theory of sound, *Nature* **119**, 553 (1927).
- [36] D. A. Wisniacki, F. Borondo, E. Vergini, and R. M. Benito, Beyond the first recurrence in scar phenomena, *Phys. Rev. E* **62**, R7583(R) (2000).
- [37] D. A. Wisniacki, F. Borondo, E. Vergini, and R. M. Benito, Localization properties of groups of eigenstates in chaotic systems, *Phys. Rev. E* **63**, 066220 (2001).
- [38] J. Pathak, Z. Lu, B. Hunt, M. Girvan, and E. Ott, Using machine learning to replicate chaotic attractors and calculate Lyapunov exponents from data, *Chaos* **27**, 121102 (2017).
- [39] J. Pathak, B. Hunt, M. Girvan, Z. Lu, and E. Ott, Model-free prediction of large spatiotemporally chaotic systems from data: A reservoir computing approach, *Phys. Rev. Lett.* **120**, 024102 (2018).